

High-redshift halo-galaxy connection via constrained simulations

ADI NUSSER¹

¹ *Department of Physics and the Asher Space Research Institute
Israel Institute of Technology Technion, Haifa 32000, Israel*

ABSTRACT

The evolution of halos with masses around $M_h \approx 10^{11} M_\odot$ and $M_h \approx 10^{12} M_\odot$ at redshifts $z > 9$ is examined using constrained N-body simulations. The specific mass accretion rates, \dot{M}_h/M_h , exhibit minimal mass dependence and agree with existing literature. Approximately one-third of simulations reveal an increase in \dot{M}_h around $z \approx 13$, possibly implying a dual-age stellar population. Comparing simulated halos with observed galaxies having spectroscopic redshifts, we find that for galaxies at $z \gtrsim 9$, the ratio between observed star formation rate (SFR) and \dot{M}_h is approximately 2%. This ratio remains consistent for the stellar-to-halo mass ratio (SHMR) but only for $z \gtrsim 10$. At $z \simeq 9$, the SHMR is notably lower by a factor of a few. At $z \gtrsim 10$, there is an agreement between specific star formation rates (sSFRs) and \dot{M}_h/M_h of halos. However, at $z \simeq 9$, observed sSFRs exceed simulated values by a factor of two. To explain the relatively high star formation efficiencies in high- z halos with $M_h \approx 10^{11} M_\odot$, a simplified model is proposed, assuming the applicability of the local Kennicutt-Schmidt law. The enhanced efficiency relative to low- z is mainly driven by the reduced effectiveness of stellar feedback due to deeper gravitational potential for halos of a fixed mass.

Keywords: cosmology: large-scale structure – galaxies: formation – galaxies: high redshift – galaxies: ISM – galaxies: luminosity function

1. INTRODUCTION

The standard Λ CDM cosmological model, incorporating a cosmological constant, Λ , and cold dark matter (DM), has been remarkably successful in interpreting and predicting fundamental properties of the large-scale structure of the Universe. Despite potential tensions (e.g. [Asgari et al. 2021](#); [Riess et al. 2023](#)), this success extends to temperature anisotropies of the cosmic microwave background (CMB), clustering of the distribution of galaxies, and deviations of galaxy motions from a purely Hubble flow (e.g. [Bennett et al. 2013](#); [Tegmark et al. 2004](#); [Cole et al. 2005](#); [Eisenstein et al. 2007](#); [Davis et al. 2011](#); [Carrick et al. 2015](#); [Planck Collaboration et al. 2018](#); [Lilow et al. 2021](#)). On galactic scales, predicting the properties of the galaxy population and its evolution with redshift has been less straightforward. This complexity arises from the intricate nature of baryonic physics involved in star formation processes, including gas dynamics, heating and cooling mechanisms, and

notably, the energetic feedback from supernovae (SN) and active galactic nuclei (AGNs) (e.g. [Larson 1974](#); [Dekel & Silk 1986](#); [White & Frenk 1991a](#); [Silk & Rees 1998](#); [Dekel et al. 2009b](#); [Okalidis et al. 2021](#); [Krumholz et al. 2018](#); [Nusser & Silk 2022](#)).

Prior to the era of the James Webb Space Telescope (JWST) ([Gardner et al. 2023](#)), significant efforts have been invested in fine-tuning models of galaxy formation to adequately describe observations at low and moderately high redshifts ($z \lesssim 10$) (e.g. [Finkelstein et al. 2022](#)).

Observations obtained with the JWST have significantly deepened our view of the universe, revealing galaxies as far back as a couple of hundred million years near the Big Bang. However, the JWST has also detected an unexpected excess of luminous galaxies at higher redshifts. While the initial findings from the JWST posed serious challenges for the standard Λ CDM model of structure formation, the severity of these discrepancies were largely alleviated with more precise calibration and the availability of spectroscopic redshifts (cf. [Yung et al. 2024](#), for an overview).

It should be emphasized that the star formation rates (SFRs) in high-redshift JWST galaxies are not particu-

larly unusual in themselves (e.g. Robertson et al. 2023; Harikane et al. 2024). These galaxies exhibit SFRs that can be adequately sustained by cosmological gas accretion onto halos (Mason et al. 2023). Matching the abundance of halos to the observed distribution of UV magnitudes (used as proxies for the SFRs) of galaxies at $z \gtrsim 10$ implies that these galaxies should be hosted in halos of mass $M_h \approx 10^{11} M_\odot$ (Boylan-Kolchin 2023; Mason et al. 2023). For such halos, the star formation efficiency f_* , i.e. the fraction of accreting gas needed account for the SFRs, is $\gtrsim 0.15$ (see 3.2.1 below). At low redshifts ($z < 4$), the stellar-to-halo mass ratio (SHMR) inferred from abundance matching is in the range 0.001–0.01 for $M_h \approx 10^{11} M_\odot$ halos (e.g. Moster et al. 2013; Rodríguez-Puebla et al. 2017; Girelli et al. 2020; Fu et al. 2022). Assuming a global gas fraction $f_b = 0.157$ in galaxies (Planck Collaboration et al. 2018), this implies an average star formation efficiency, $f_* \approx 0.06 - 0.006$, which is at least a factor of two lower than the inferred value at $z > 10$.

Additionally, uncertainties in estimated stellar masses remain large even for best observed objects. Different assumptions in the star formation history (SFH) in SED fitting can lead to non-negligible differences of the stellar masses Whitler et al. (2023); Pacifici et al. (2023); Wang et al. (2023). This is the case for example for the galaxy GS-z12 with a spectroscopic redshift $z = 12.48$ (D’Eugenio et al. 2023). Using the PROSPECTOR SED fitting (Johnson et al. 2021), H24 found a stellar mass $M_* = 4.3_{-2}^{+1.8} \times 10^8 M_\odot$ for this galaxy, while analysis using the BEAGLE core (Chevallard & Charlot 2016) performed by D’Eugenio et al. (2023) lead to $M_* = 4.36_{-1.27}^{+1.8} \times 10^7$ for the same object.

The evolution of the SHMR inferred through abundance matching techniques is sensitive to various factors, including the shape of the galaxy stellar mass function (e.g. Yang et al. 2012) As highlighted by Fu et al. (2022), uncertainties in the observed stellar mass functions at redshifts $z < 4$ can lead to differing interpretations regarding the evolution of the SHMR from redshift $z = 0$ to $z = 4$. Depending on specific assumptions made about the stellar mass function, the SHMR could exhibit either a decrease or an increase over this redshift range. For instance, for a halo with $M_h \approx 10^{11} M_\odot$, the SHMR could vary by two orders of magnitude. Seen in this light, it entirely plausible that the inferred star formation efficiency varies between low and high redshifts. The key question is whether galaxy formation can account for the boost in efficiency at high redshifts.

Numerous models aim to understand the formation of luminous high-redshift galaxies. Harikane et al. (2023) suggested that the SFR inferred from UV luminosities

might be overestimated because of a prevalence of a top-heavy initial stellar mass function (IMF) at high redshift. Such a top-heavy IMF could arise naturally in the low metallicity environment characteristic of Population III stars. Furthermore Yung et al. (2024) emphasized that a top-heavy IMF could account for a factor of 4 boost in the UV luminosities, which is needed to bring their semi-analytic models to agree with observations.

Another model predicts a feedback-free star formation at high redshifts. Dekel et al. (2023) present a set of conditions on the gas density and surface density that allow for a feedback-free star formation in gas clouds of $\approx 10^7 M_\odot$ at high redshifts. At $z \approx 10$, the conditions are satisfied in halos of mass $10^{11} M_\odot$. The high SFR efficiency depletes most the gas in the galaxy, effectively halting star formation until enough new gas mass is accumulated by accretion and the next episode of star formation is initiated.

However, Silk et al. (2024) invoke AGN positive feedback to explain the elevated SFR. They propose that a short-lived AGN activity triggers vigorous star formation activity in high redshift galaxies via the generation momentum-conserving outflows. They predict that a late transition to energy-conserving flows at $z \approx 6$ is associated with gas depletion and hence quenched star formation at low redshifts.

According to Ferrara et al. (2023) the high abundance of $z \gtrsim 10$ galaxies could be explained if dust attenuation is decreased at high relative to lower redshifts, in such a way that it compensates for the reduced abundance of the host halos.

Moreover, there is a growing evidence for a highly variable star formation history at high redshifts (Cole et al. 2023; Dressler et al. 2024). The variability could be attributed to a combination of factors, including mergers, interactions, and environmental conditions. The variability could bias the inferred UV luminosity function as well as the stellar masses (Sun et al. 2023a,b). The reason is that galaxies residing in low mass halos are likely to be preferentially detected during phases of increased star formation, which are associated with heightened production of UV photons. Consequently, these galaxies might seem less numerous than they actually are. This also could overestimate the inferred stellar mass. However, the required variability for explaining the observations seems to exceed the predictions of simulations (Pallottini & Ferrara 2023), but see (Sun et al. 2023b).

In vanilla semi-analytic galaxy formation models (SAMs) (e.g. Kauffmann et al. 1993; Benson 2010; Cora 2006; Henriques et al. 2015; Somerville & Davé 2015), the SHMR versus halo mass is almost independent of

redshift (Mitchell et al. 2018; Yung et al. 2024), suggesting that efficiency with which gas converts into stars relative to the mass of their associated dark matter halos remains relatively constant throughout the cosmic history. According to these models, the expected star formation efficiency stars in a $10^{11} M_{\odot}$ halo is approximately 10^{-3} (e.g. Mitchell et al. 2018; Yung et al. 2024), which is an order of magnitude lower than the efficiency required at $z \gtrsim 10$.

Another potential challenge is that the observed galaxy sizes tend to be larger than expected in models for structure formation (Baggen et al. 2023; Robertson et al. 2023). We argue in §5 that if gas resides in clumpy disks then angular momentum transfer from the disk to the DM halo can be achieved by dynamical friction (Chandrasekhar 1949; El-Zant et al. 2001; Dekel et al. 2009a).

Numerical studies of individual objects typically rely on the methodology of zoom-in simulations (e.g. Katz et al. 1993; Libeskind et al. 2020; Grand et al. 2021; Sun et al. 2023b; Pallottini & Ferrara 2023). In this type of simulations high resolution is employed only in a small region allowing a detailed study of its small scale dynamics while simultaneously capturing the interaction within the larger cosmic environment. In this paper we invoke an alternative approach of constrained simulations to model the high redshift $z > 9$ accretion history of halos above $M_h \approx 10^{11} M_{\odot}$. We utilize the Hoffman & Ribak (1991) method of constrained random realizations to generate initial conditions that are guaranteed to contain a halo in specified mass range, when evolved forward to a specified redshift, z .

The technique of constrained simulations is very useful in large scale structure studies, especially for assessing uncertainties in parameter estimations realistically and in mitigating cosmic variance (Hellwing et al. 2017). This approach has been used to derive simulation initial conditions from the observed peculiar velocities (Hoffman et al. 2015) and from the 2MRS redshift survey (Lilow et al. 2021). Initial conditions based on the galaxy distribution in the Sloan Digital Sky Survey (SDSS) survey have also been generated to run a constrained simulation to study the local Universe (Wang et al. 2016). The same simulation has also been utilised to study the $z \simeq 0$ descendants of galaxies at $z \approx 8 - 9$ galaxies (Chen et al. 2023).

The structure of the paper is outlined as follows. In §2, we assess the abundance of halos and compare it with the luminosity function of galaxies at high redshifts. We underscore the advantage of constrained simulations based on the expected abundance of the host halos. The simulations are detailed in §3, which in-

cludes the method for generating suitable initial conditions. Additionally, this section contrasts the accretion history of halos in the simulations with observational data. In §4, a straightforward model for star formation is introduced. The model produces a significantly higher ratio of stellar to halo mass at high redshifts compared to low redshift. Further, in §5 we present arguments that dynamical friction of galactic disks at high redshift could lead to a reduction of the effective radii of galaxies by decelerating the rotation of the disk. A summary and discussion are provided in §6.

We adopt the standard flat Λ CDM cosmological model (Planck Collaboration et al. 2018) with a total mass density parameter $\Omega_m = 0.311$, baryonic density $\Omega_b = 0.049$, Hubble constant $H_0 = 67.7 \text{ km s}^{-1} \text{ Mpc}^{-1}$ and normalization $\sigma_8 = 0.81$.

2. HALO ABUNDANCE AT HIGH REDSHIFT

Figure 1 displays the abundance of DM halos per logarithmic bins per Mpc^3 at different redshifts. We employ a halo definition in terms of a spherical overdensity, where the halo virial radius $r_h(t)$, at any given time t is determined such that the mean density within this radius equals 200 times the critical density of the universe, $\rho_c(t) = 3H(t)^2/8\pi G$. Therefore,

$$\begin{aligned} r_h(t) &= 0.1H(t)^{-1}V_c, \\ M_h(t) &= 0.1G^{-1}H(t)^{-1}V_c^3, \end{aligned} \quad (1)$$

where the circular velocity $V_c = \sqrt{GM_h/r_h}$. At high redshifts where $H \sim 1/t$, these relations yield

$$\begin{aligned} r_h(t) &= 13.1 \text{ kpc} \left(\frac{11}{1+z} \right)^{3/2} \frac{V_c}{181 \text{ km s}^{-1}}, \\ M_h(t) &= 10^{11} M_{\odot} \left(\frac{11}{1+z} \right)^{3/2} \left(\frac{V_c}{181 \text{ km s}^{-1}} \right)^3, \end{aligned} \quad (2)$$

The plots are generated using the mass function outlined by Tinker et al. (2008) for the Λ CDM cosmological model, as incorporated within the COLOSSUS cosmology Python package (Diemer 2018). The curves corresponding to halos within the mass range $M_h \gtrsim 10^{11} M_{\odot}$ at redshifts $z \gtrsim 9$ exhibit comparable abundance to large groups and clusters at $z = 0$. At the upper end of the mass range, the dependence on mass steepens significantly at such high redshifts. For instance, at $z = 9$, the abundance of halos with $M_h = 10^{12} M_{\odot}$ is four orders of magnitude lower than halos with $M_h = 10^{11} M_{\odot}$. The dashed lines represent the following simple approximation to the mass function

$$\frac{dn(z, M_h)}{d \log M_h} = \frac{10^{-5} \text{ Mpc}^{-3}}{\left[\left(\frac{M_h}{M_{-5}(z)} \right)^2 + 0.25 \left(\frac{M_h}{M_{-5}(z)} \right)^{0.8} (z) \right]^2}.$$

(3)

The approximation is valid in the redshift range $10 < z < 20$ with $M_{-5}(z)$ is defined as,

$$\log(M_{-5}/10^{11} M_{\odot}) = 0.185(z - 10)^{1.03}, \quad (4)$$

and is equal to the halo mass where $dn/d\log M = 10^{-5} \text{ Mpc}^{-3}$. For $M \gtrsim M_{-5}(z)$, we have the steep dependence $dn/d\log M \sim M^{-4}$.

Various fitting formulae for the mass function are available in the literature (e.g. Press et al. 1974; Sheth & Tormen 1999; Jenkins et al. 2001; Angulo et al. 2012; Seppi et al. 2021). These formulas are primarily calibrated using low redshift outputs from simulations, although exceptions exist (see Behroozi et al. (2013)). Therefore, it is important to investigate whether discrepancies among these mass functions might be particularly notable when applied to high redshifts.

In fig. 2, compare the Tinker et al. (2008) with the widely used Despali et al. (2016) mass function by examining the ratio of the latter to the former as a function of halo mass. The depicted curves represent two specific redshift values, as indicated in the figure. The disparity between the two mass functions grows with both mass and redshift, albeit remaining within a factor of a few. This discrepancy remains modest compared to the uncertainty in the abundance of observed galaxies at $z \gtrsim 10$. Indeed, we have conducted numerous analyses using the Despali et al. (2016) mass function and found negligible changes in the relevant results.

Galaxies observed at high redshifts are linked with halos having masses $M_h \approx 10^{11} M_{\odot}$ (e.g., Boylan-Kolchin 2023; Chen et al. 2023; Yung et al. 2024). This connection is established through abundance matching, where the galaxy UV luminosity function is mapped to the halo mass function. Specifically, this involves equating the cumulative number density of galaxies with UV magnitudes above a given value M_{UV} to the number density of halos with masses greater than M_h .

Harikane et al. (2024) (hereafter H24) constrain the UV luminosity function of high-redshift galaxies using 25 galaxies with spectroscopic redshifts spanning $z \approx 8.61 - 13.20$. Their constraints align with various luminosity distributions derived from photometric redshifts (e.g., Pérez-González et al. 2023; Donnan et al. 2023; Harikane et al. 2023; Bouwens et al. 2023). H24 show that the observed UV luminosity distribution can be effectively modeled by a double power-law function, denoted as Φ_{UV} . We have verified (not shown here) that this fit also agrees with the observed luminosity functions in Yung et al. (2024).

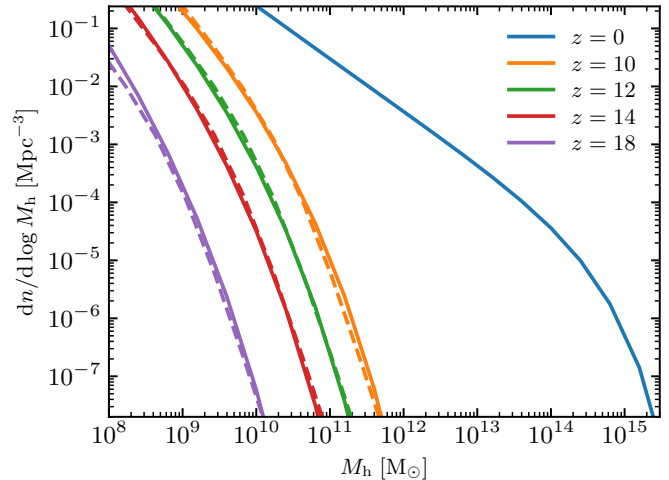


Figure 1. Halo abundance versus mass at different redshifts as denoted in the figure. The solid lines are derived from the Tinker et al. (2008) expression for the mass function in the Planck Λ CDM cosmology (see text). Dashed lines are obtained from the fit eq. (3). At the high mass end, the curves are $\sim M_h^{-4}$ and thus the cumulative number density $n(> M_h) \approx (1/4)dn/d\log M_h$

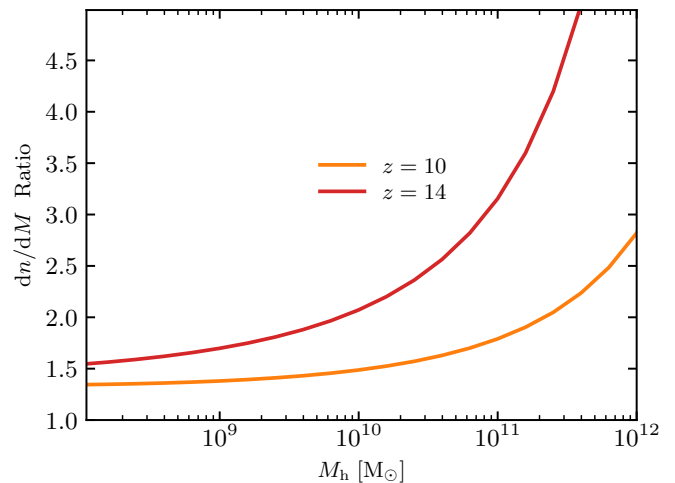


Figure 2. Ratio of Despali et al. (2016) to Tinker et al. (2008) mass functions

Using this double power-law fit, we conduct a straightforward abundance matching to associate galaxies with a UV magnitude, M_{UV} , to halos of mass M_h

The results of the abundance matching are summarized in fig. 3 for three redshift values. The width of the shaded area corresponds to variation in the normalization of the double power law fit, spanning a factor in between 0.2 and 5. While this should provisionally

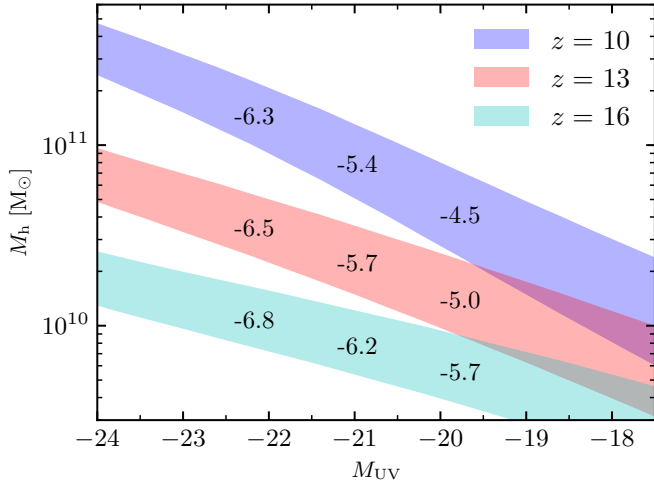


Figure 3. Halo mass versus UV magnitude obtained by abundance matching of the Tinker et al. (2008) halo mass function and the power law fit of H24 to UV luminosity function, Φ_{UV} . Each shaded area corresponds to a single redshift and is bounded by M_h curves obtained using $5\Phi_{UV}$ (yielding the lower boundary of the shaded area) and by $0.2\Phi_{UV}$ (leading to the upper boundary). The numbers in each shaded area represent the log of the cumulative halo abundance (in Mpc^{-3}) expected at the corresponding M_h .

reflect the uncertainty in the measured UV luminosity function of H24, it is important to note that the uncertainty in the observed luminosity in a single bin of one UV magnitude width could be as large as two orders of magnitude.

At $M_{UV} = -21$, the halo mass is in the range $M_h = 6 \times 10^{10} - 1.5 \times 10^{11} M_\odot$ at $z = 10$, with a cumulative halo abundance (indicated by log the number density in the shaded areas) similar to massive groups and clusters at $z = 0$. Although galaxies with a fixed M_{UV} correspond to lower halo masses as we move from low high redshifts, the decrease in halo mass is insufficient to maintain the same abundance. In fact, halos corresponding to a fixed M_{UV} become rarer.

At $z \approx 10$, on average only a single halo with $M_h = 2 \times 10^{11} M_\odot$ is expected in a box a 100 Mpc. While it is possible to employ zoom-in techniques for simulating massive halos at $z \gtrsim 10$, this necessitates significant computational resources. Instead, we adopt a computationally friendlier approach, utilizing constrained random realizations to generate initial conditions that are guaranteed to contain a massive halo when evolved forward to a specified redshift, z .

3. SIMULATIONS

In 3.1, we outline the method for generating constrained initial conditions. Using these initial conditions, simulations of dark matter particles were conducted in periodic boxes using the SWIFT cosmological code (Schaller et al. 2023). All simulations started at redshift $z_i = 80$ and concluded at $z = 9$.

We performed nine simulations constrained to have halo masses of approximately $M_h \approx 10^{11} M_\odot$ in boxes of $L = 17.1$ Mpc, along with one unconstrained simulation in a box of the same size. Additionally, two simulations were conducted with initial conditions constrained to include a halo mass of $M_h \approx 10^{12} M_\odot$ at $z = 9$, positioned at the center of cubic boxes of $L = 36.9$ Mpc.

Each simulation consisted of 512^3 equal-mass particles, resulting in particle masses of $10^7 M_\odot$ and $10^6 M_\odot$ in the large and small boxes, respectively. The maximum physical softening used in the simulations was 100 pc. Throughout each simulation run, the output of positions and velocities of all particles was retained at 18 different redshifts spanning from $z = 20$ to $z = 9$. Halos were identified from the simulation outputs utilizing the VELOCIRAPTOR halo finder (Elahi et al. 2019). This halo finder provides halo masses according to several definitions. Here we use VELOCIRAPTOR masses that match the definition in eq. (1).

3.1. Constrained Initial Conditions

We formulate the condition (constraint) for the presence of a halo of a given mass as follows. Let $\delta(\mathbf{x}, z)$ be the linearly evolved density at redshift z and $\delta_R(\mathbf{x}, z)$ be the convolution of δ with a top-hat window of comoving radius R . We associate a halo of mass M_h with a comoving Lagrangian radius $R_L = (3M_h/4\pi\rho_m)^{1/3}$, where ρ_m is the background density in comoving coordinates.

The formation of a halo of mass M_h at redshift z , located at position at \mathbf{x}_0 is determined by the condition $\delta_{R=R_L}(\mathbf{x}_0, z) = \delta_c \simeq 1.68$ (e.g. Press & Schechter 1974; Peebles 1980). Here, δ_c serves as a critical threshold indicative of the collapse or virialization of dark matter halos. At $z = 10$, halos with masses $M_h = 10^{11} M_\odot$ and $M_h = 10^{12} M_\odot$ correspond to Lagrangian comoving radii $R_L = 0.84, \text{Mpc}$ and $1.82, \text{Mpc}$, respectively. In terms of the ratio δ_c/σ_{R_L} , these values equate to 4.8 and 6.5. This ratio provides a measure of the likelihood of halo formation under the specified conditions.

This formulation is only approximate as the superposition of generic fluctuations on all scales and non-linear evolution will lead to deviations from the desired halo mass and position. Nonetheless, the prescription is reasonable for massive (rare) halos (Robertson et al. 2009; Ludlow et al. 2014), as is the case in the current study.

We adopt the methodology of Hoffman & Ribak (1991) to generate gaussian random fields that satisfy the aforementioned condition. This elegant method expresses the constrained random field, denoted by δ_1 , in terms of an unconstrained random gaussian field, δ^{unc} , as follows

$$\delta_1(\mathbf{x}, z) = \delta^{\text{unc}}(\mathbf{x}, z) - \langle \delta(\mathbf{x}, z) | \delta_{RL}^{\text{unc}} \rangle + \langle \delta(\mathbf{x}, z) | \delta_c \rangle \quad (5)$$

where δ_{RL}^{unc} is the value of the filtered unconstrained field at \mathbf{x}_0 .

The ensemble average of all δ fields satisfying the constraint $\delta_{RL}(\mathbf{x}_0, z) = C$ is given by

$$\langle \delta(\mathbf{x}) | C \rangle = \zeta(|\mathbf{x} - \mathbf{x}_0|) \frac{C}{\sigma_{RL}^2}, \quad (6)$$

where σ_{RL}^2 is the variance of the smoothed density, δ_{RL} .

3.2. Results

We begin by visually inspecting the projected (2D) density field in one of the constrained simulations. Figure 4 illustrates the 2D density (in units of the mean 2D density value) for one of the $M_h = 10^{11} M_\odot$ constrained simulations. The overlaid circles represent identified halos in different mass ranges, as described in the figure caption. Only halos above $10^9 M_\odot$ are marked.

The displayed region of the box is focused around the center. As expected, the most massive halo (MMH) forms near the center. Additional massive halos are associated with the growth of the MMH, however, their masses are significantly lower than the MMH. Halos in the mass range $5 \times 10^9 < M_h/M_\odot < 10^{10}$ (red circles) are present at $z \simeq 12$. These halos are not considered rare, as their expected abundance is $10^{-2} - 10^{-3} \text{dex}^{-1} \text{Mpc}^{-3}$ (see fig. 1). Therefore, we expect to identify a few such halos even in our simulation box of $L = 17.1 \text{Mpc}$.

Inspection of the panels at $z = 11$ and $z = 10$ reveals a major merger event with the two halos marked by two blue circles ($10^{10} < M_h/M_\odot < 5 \times 10^{10}$) at $z = 11$ merging to form the larger halo indicated by the white circle ($5 \times 10^{10} < M_h/M_\odot < 10^{11}$) at $z = 10$. There is a clear tendency of increasing halo mass as we move nearer to the MMH, particularly at the lowest redshifts.

Figure 5 plots the abundance of halos from the simulations as a function of M_h . At the high mass end, the simulated abundance is significantly above the predictions from the Tinker et al. (2008) fitting formula (green curve). In both $M_h = 10^{11} M_\odot$ and $M_h = 10^{12} M_\odot$ constrained simulations, the MMH is associated with other relatively rare massive halos with abundance well above the green curve.

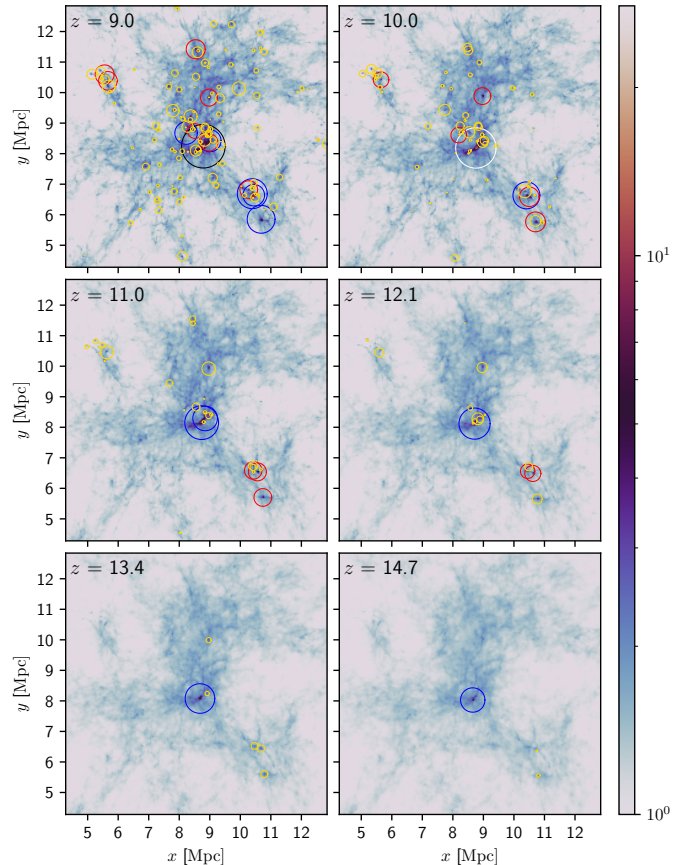


Figure 4. Projected 2D density field computed from one of the constrained simulations with $L = 17.1 \text{Mpc}$ at six distinct redshifts. Circles denote halos classified by mass ranges: black ($M_h/M_\odot > 10^{11}$), white ($5 \times 10^{10} - 10^{11}$), blue ($10^{10} - 5 \times 10^{10}$), red ($5 \times 10^9 - 10^{10}$), and yellow ($10^9 - 5 \times 10^9$), with size logarithmically scaled by mass. The color bar indicates density in units relative to the mean density within the simulation box.

3.2.1. Halo Accretion History

The halo accretion history is directly linked to the availability of gas for star formation. Newly accreted gas replenishes the reservoir, which is subsequently converted into stars and may escape the galaxy through processes like supernovae (SN) and active galactic nuclei (AGN) feedback.

Figure 6 displays curves of the accretion histories of the MMH in all simulations. The top, middle and bottom panels correspond, respectively, to the halo mass versus time $M_h(t)$, the accretion rate \dot{M}_h , and the specific accretion rate \dot{M}_h/M_h . Squares and circles represent quantities inferred from observed data, as detailed below.

The curves of $M_h(t)$ (top panel) reveal that half of the simulated halos, including the unconstrained halo (dot-

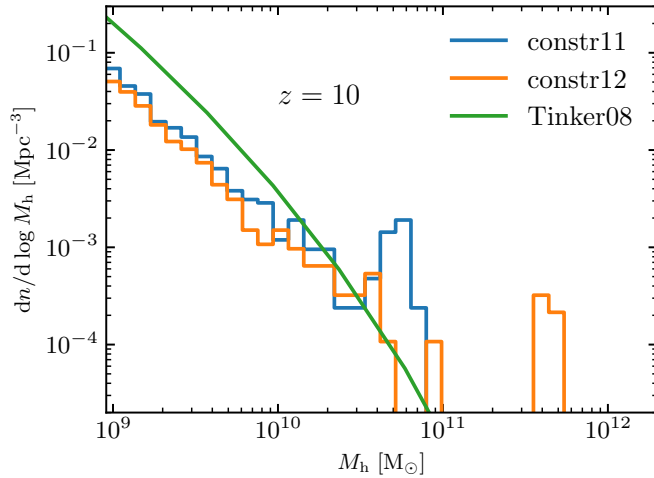


Figure 5. Halo abundance computed from the simulations output at $z = 9$. The blue and orange histograms represent the constrained simulations with halo masses of $10^{11} M_{\odot}$ and $10^{12} M_{\odot}$, respectively. The green curve depicts the Tinker et al. (2008) mass function.

ted), have acquired 80% of their final masses in the last 150 Myr. Only the dashed curves, corresponding to constrained simulations with $M_h \approx 10^{12} M_{\odot}$ and one of the nine solid curves, have acquired a mass $\gtrsim 10^{10} M_{\odot}$ by $z = 15$. Significant variations exist between individual halos, evident from the curves of \dot{M}_h (middle panel), where some halos exhibit fluctuating M_h while others (e.g., dashed and a few solid curves) display smoother behavior, albeit with fluctuations at a $\lesssim 100$ Myr scale.

The cyan circles in the top panel represent halo masses inferred via abundance matching from the observed UV magnitudes, M_{UV} , of galaxies listed in table 1 of H24. We refrain from attaching error bars to these estimates due to uncertainties in abundance matching, which are relatively small compared to the scatter of the points. The cyan points fall within the range of solid curves corresponding to simulations constrained to contain a $M_h \approx 10^{11}$ halo. While this is expected given that the choice of this mass motivated by the observed abundance of galaxies, the result is not entirely trivial. At a given redshift, the spread in halo masses between different simulations is large, ranging from $M_h \approx 10^{10} M_{\odot}$ to $10^{11} M_{\odot}$ at $z = 10$, as indicated by the solid curves. This mass range is associated with more than a two-order-of-magnitude difference in the abundance of halos, as shown in fig. 1.

Using SED fitting, H24 provide SFRs and stellar masses for a subset of the galaxies in table 1 of their paper. The magenta squares in the top panel are halo masses estimated from these stellar masses (table 3 in

H24) assuming

$$M_h = f_t^{-1} M_*, \quad (7)$$

where $f_t = f_* f_b$ is assigned the value $f_t = 0.02$ and the error bars in the figure are estimated from the uncertainties on M_* . The open square symbols refer to the galaxy GS-z12 for which different values of redshift, SFR and M_* are reported in D’Eugenio et al. (2023) and H24. Both sets of data are shown with D’Eugenio et al. (2023) being the point with the lower redshift ($z = 12.43$).

At $z \gtrsim 10$, halo masses inferred from observed stellar masses (magenta squares) by eq. (7) are consistent with the constrained simulations with $M_h \approx 10^{11} M_{\odot}$ and the results from abundance matching (cyan points). However at $z \simeq 9$, the estimate in eq. (7) falls below the simulation and abundance matching. Decreasing the parameter f_t by a factor of $\approx 5 - 10$ would bring the $z \simeq 9$ galaxies to agree with the simulations and abundance matching. This is in line with the finding of Yung et al. (2024) that the luminosity function predicted by their semi-analytic models is consistent the observations well at $z \lesssim 9$, while it underestimates the observed abundances at $z \approx 11$.

The UV magnitudes, M_{UV} , of galaxies in table 1 of H24 can also be used to deduce the SFRs using $\dot{M}_* = 1.15 \times 10^{-28} L_{UV}$. The time derivative of eq. (7) relates the SFR, \dot{M}_* , to the halo accretion rate as $\dot{M}_h = \dot{M}_*/f_t$. The results for $f_t = 0.02$ are plotted as cyan points in the middle panel.

In addition to M_{UV} , the SED-fitted SFRs in table 3 of H24 are used here to obtain \dot{M}_h , also for $f_t = 0.02$. The results are represented as the magenta squares in the middle panel. The UV magnitude and SED-based value of \dot{M}_h agree with each other, but are not identical, as the SED fitting involves a more detailed modeling of the SFR than the UV magnitudes alone. Curves of accretion rates from the $M_h = 10^{11} M_{\odot}$ constrained simulations, are consistent with the observations via M_{UV} (cyan) and SED-SFRs (magenta). Compared to the top panel, halo masses inferred from the observed stellar masses (magenta square) are below those predicted through abundance matching (cyan). It is important to note that while both the cyan and magenta points in the top and middle panels rely on M_{UV} , their underlying methodologies differ - abundance matching for the top panel versus an empirical SFR- M_{UV} relationship for the middle panel.

The results at $z \simeq 9$ are intriguing. While the choice of $f_t = 0.02$ for inferring M_h from M_* (top panel) and \dot{M}_h from \dot{M}_* (middle panel) matches well the $M_h = 10^{11} M_{\odot}$ simulations at $z \gtrsim 10$, a lower f_t is needed for consistency at $z \simeq 9$. However, the deviations in M_h derived

from simulations at $z \simeq 9$, when compared to observational inferences, are about 2 – 4 times larger than those seen in \dot{M}_h at the same redshift. This discrepancy is clearly illustrated in the specific accretion rates shown in the bottom panel.

The bottom panel shows the specific halo accretion rates, \dot{M}_h/M_h , from simulations. These rates hover around a simple fit denoted by a black line, represented by the equation $\text{dln}M_h/\text{dt} = 3.15t_{\text{Gyr}}^{-4/3} \text{Gyr}^{-1}$. This fit approximates the mean accretion rate for halos of mass $M_h = 10^{11} M_\odot$ as proposed by Fakhouri et al. (2010).

The magenta squares in the bottom panel indicate the sSFR of galaxies as catalogued in table 3 of H24. There is a reasonable match between the observed sSFRs (magenta squares) and the specific halo accretion rates from the simulations at $z > 10$. This consistency with the simulations corroborates the findings of Bouwens et al. (2023), who noted that the sSFRs tend to follow the scaling $(1+z)^{2.5}$ proposed by Fakhouri et al. (2010) for the specific halo accretion rate at high redshift. However, it is important to note that the normalization of the specific halo accretion rate in Bouwens et al. (2023) is higher by a factor of a few compared to the fit by Fakhouri et al. (2010).

According to equation eq. (7), the specific accretion rate is equal to the sSFR, i.e. $\dot{M}_h/M_h = \dot{M}_*/M_*$, independently of f_t . Note that $M_* \propto M_h^\alpha$ ($\alpha = \text{const}$), then $\dot{M}_h/M_h = \alpha^{-1} \dot{M}_*/M_*$ (Behroozi & Silk 2015). Therefore, also for $\alpha \neq 1$ curves of the sSFR and the specific halo accretion rate should trace each other, with a constant ratio between them.

4. A SIMPLIFIED MODEL FOR STAR FORMATION

We present a straightforward model that offers insights into certain aspects of galaxy formation at high redshifts. Our primary argument is that star formation processes at both high and low redshifts may not significantly differ. Given a halo with of mass $M_h(t_z)$ at a time t_z corresponding to a redshift z , we develop a model to calculate the stellar mass, M_* , and the the SFR \dot{M}_* , within this halo. The main assumption of our model is that star formation at high redshift occurs in a rotationally supported disk, governed by the Schmidt-Kennicutt (SK) law, as deduced from observations in the local universe (Schmidt 1959; Kennicutt 1998). At a specific time t and for a disk radius R , let $\Sigma_g(t, R)$ and $\Sigma_*(t, R)$ denote the surface densities of the disk's gaseous and stellar components, respectively. We express the SK law as follows

$$\dot{\Sigma}_* = A \Sigma_g^n, \quad (8)$$

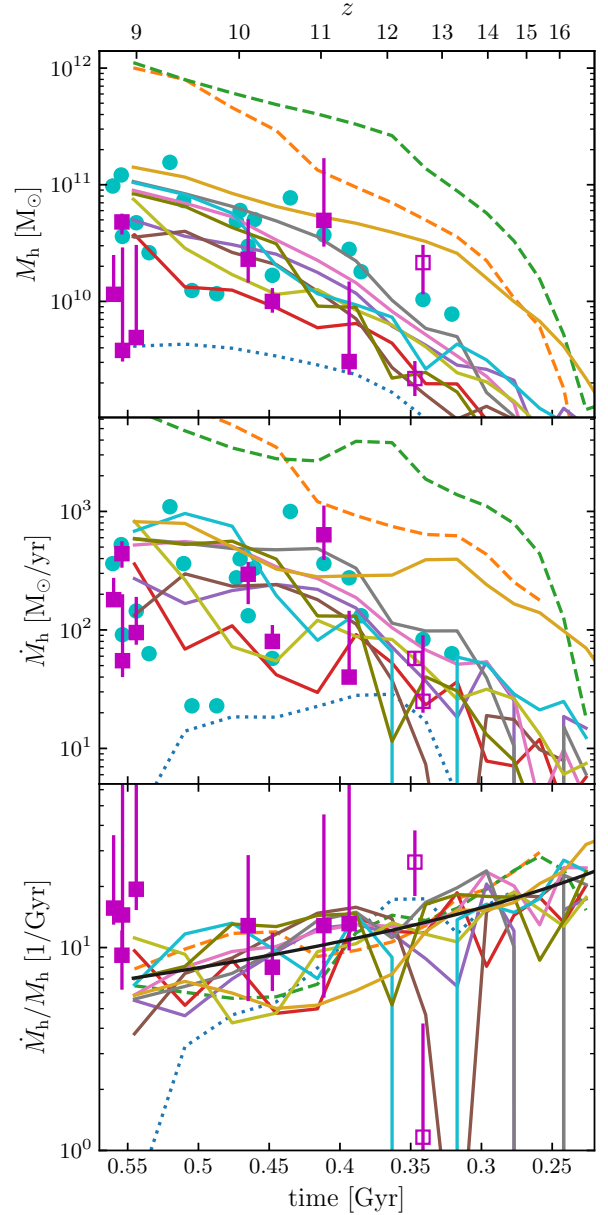


Figure 6. Accretion histories of the main halos in the simulations. The dotted line represents the unconstrained simulation, while solid and dashed lines correspond to constrained simulations with $M_h = 10^{11} M_\odot$ and $10^{12} M_\odot$, respectively. *Top:* mass as a function of time. Magenta squares are based on the observed M_* using eq. (7). Cyan circles represent M_h obtained by abundance matching from observed M_{UV} . *Middle:* The accretion rate \dot{M}_h . Squares represent $\dot{M}_h = f_t^{-1} \dot{M}_*$ derived from observed \dot{M}_* . The cyan circles show results obtained from the \dot{M}_* estimated from UV magnitudes directly. *Bottom:* Squares show the sSFR, \dot{M}_*/M_* , of observed galaxies. Open squares refer to the galaxy GS-z12 (see text). The black curve is a fit $\sim t^{-4/3}$.

where $\dot{\Sigma}_*$ is the SFR per unit area of the disk. We adopt the parameters, $n = 1.54$ and $A = 10^{-3.95}$ (Kennicutt & De Los Reyes 2021) where Σ_{SFR} and Σ_g are, respectively in units of $M_\odot \text{pc}^{-2}$ and $M_\odot \text{pc}^{-2}$.

The basic picture is as follows. The gas already present in the disk undergoes partial conversion into stars following the SK law, accompanied by subsequent stellar feedback (SN and winds) that expels a fraction of the gas mass. Additionally, the reservoir of gas in the disk is replenished and expanded as the halo accretes additional matter.

The application of the SK law requires the gas surface density $\Sigma_g(t, R)$ as a function of time and radius. This is expressed through the mass balance equation,

$$\dot{\Sigma}_g = \dot{\Sigma}_{\text{acc}} - \dot{\Sigma}_* - \dot{\Sigma}_{\text{ej}}, \quad (9)$$

where $\dot{\Sigma}_{\text{acc}}$ denotes the added baryonic mass to the disk surface density due to accretion onto the halo, $\dot{\Sigma}_*$ is the rate of gas mass converted into star, and $\dot{\Sigma}_{\text{ej}}$ represents the gas ejected from disk by stellar feedback. We restrict the model to halos of mass $\lesssim 10^{12} M_\odot$, where AGN feedback is considered subdominant (e.g. Croton et al. 2006; Bower et al. 2006; Puchwein & Springel 2013).

The ejected mass rate is expressed in terms of the circular velocity of the host halo as (e.g. White & Frenk 1991b; Kauffmann et al. 1993; Mitchell et al. 2018; Yung et al. 2019)

$$\dot{\Sigma}_{\text{ej}} = \left(\frac{V_c}{V_{\text{SN}}} \right)^{-\gamma} \dot{\Sigma}_*. \quad (10)$$

This relation implies that stellar feedback is more effective in halos with a shallow gravitational potential (Larson 1974; Dekel & Silk 1986). Mitchell et al. (2018) adopt the $V_{\text{SN}} = 380 \text{ km s}^{-1}$ and $\gamma = 3.2$ while Yung et al. (2019) use the parameters $V_{\text{SN}} = 240 \text{ km s}^{-1}$ and $\gamma = 2.8$, resulting in a comparatively weaker feedback.

We now detail our approach for estimating $\Sigma_{\text{acc}}(t, R)$. Given the halo mass $M_h(t)$ as a function of time, and consequently, through eq. (1), the halo virial radius $r_h(t)$ and circular velocity $V_c(t)$, we determine the gas mass accreted within a short time interval δt as,

$$\delta M_{\text{acc}} = f_b \dot{M}_h \delta t. \quad (11)$$

Due to the short crossing time in high-redshift halos (e.g., $t_{\text{cross}} \approx r_h/V_c = 0.1/H = 70, \text{ Myr}$ at $z = 10$) and efficient gas cooling (Dekel et al. 2023; Yung et al. 2024), we assume that δM_{acc} quickly settles into the disk, with a surface density distribution given by,

$$\delta \Sigma_{\text{acc}}(t, R) = \delta \Sigma_0 e^{-R/R_d(t)}, \quad (12)$$

where $R_d(t)$ could be a general function of t , but we rely here on the approximation (Mo et al. 1998; Yang et al.

2023),

$$R_d = 0.7 \lambda_B r_h, \quad (13)$$

where λ_B is the halo spin parameter λ_B (Bullock et al. 2001). The constant $\delta \Sigma_0$ is determined by equating δM_{acc} to the total added mass to the disk as derived by integrating over eq. (12). This yields,

$$\delta M_{\text{acc}} = 2\pi \delta \Sigma_0 R_d^2(t). \quad (14)$$

Thus, from eqs. (11) to (14), we obtain,

$$\dot{\Sigma}_{\text{acc}}(t, R) = \frac{f_b \dot{M}_h}{2\pi R_d^2(t)} e^{-R/R_d(t)}. \quad (15)$$

For the halo growth rate, we assume $\dot{M}_h/M_h \propto t^{-4/3}$ as represented by the smooth black curve in fig. 6, yielding the form,

$$M_h(t) = M_h(t_z) e^{A(t_z^{-\beta} - t^{-\beta})}, \quad (16)$$

where $A = -8.1$, $\beta = 1/3$ and t is in units of Gyr. Although we only present results for this particular choice of $M_h(t)$, we have also tested $\dot{M}_h/M_h \propto t^{-5/3}$, similar to (Fakhouri et al. 2010), and found no significant differences in the SHMR.

We perform a numerical integration of eqs. (8) and (15) from an initial time $t = t_i \ll t_z$ to $t = t_z$. We set the initial conditions as $\Sigma_*(t_i, R) = 10^{-3} \Sigma_g(t_i, R)$, where $\Sigma_g(t_i, R)$ follows an exponential disk profile. The scale length of the disk at t_i , $R_d(t_i)$, is determined according to eq. (13) with $r_h = r_h(t_i)$. The total initial gas mass in the disk is equal to $f_b M_h(t_i)$ minus the initial mass in stars. In all numerical calculations, we maintain $\lambda_B = 0.035$ in eq. (13).

In fig. 7, the SHMR is plotted against halo mass for three redshift values, z . The model incorporating the feedback parameters of Yung et al. (2019), depicted with solid curves, agrees reasonably well with the observed local SHMR as estimated through abundance matching techniques, according to studies such as (e.g. Moster et al. 2013; Rodríguez-Puebla et al. 2017; Moster et al. 2020; Shuntov et al. 2022; Girelli et al. 2020). The dashed curve for $z = 0$, which represents the stronger feedback with parameters from (Mitchell et al. 2018), shows that our model underestimates the local SHMR by nearly an order of magnitude at a halo mass $\approx 10^{11} M_\odot$.

The model SHMR acquires larger values at higher redshifts for a given mass. This is due to the relation $V_c \sim M_h/t$, indicating that a higher circular velocity V_c occurs at earlier times for a fixed M_h , leading to less efficient SN feedback and, consequently, a larger gas reservoir for star formation. For the solid curves, the SHMR

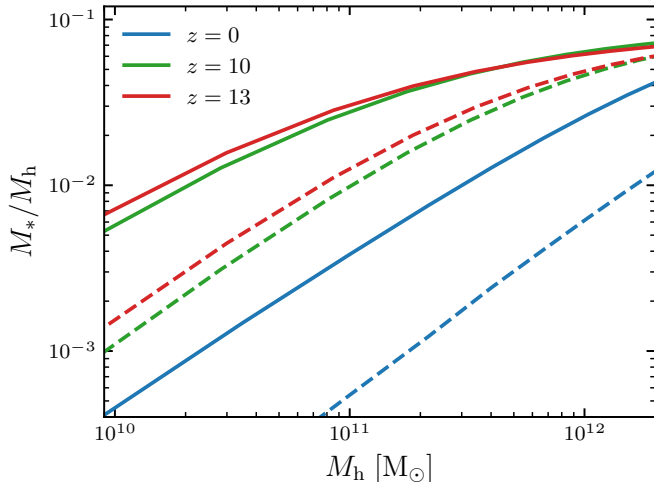


Figure 7. The SHMR from the simplified model at three different redshifts, as indicated in the figure. Dashed and solid curves correspond to strong and weak feedback recipes, respectively.

for $M_h \approx 10^{11} M_\odot$ increases by approximately an order of magnitude at high redshifts compared to $z = 0$, while for $10^{10} M_\odot$, the increase is about a factor of 25. In contrast, predictions from the UNIVERSEMACHINE (Behroozi et al. 2020) suggest that the SHMR increases by about a factor of 10 from $z = 0$ to $z = 12$ for halos with $10^{10} M_\odot$ (their figure 12).

5. SIZES

The compactness of high-redshift galaxies have been identified as a potential challenge for theoretical models. Observational estimates for the half-light radius, r_e , are available for some galaxies at high redshifts. Baggen et al. (2023) measure $r_e \approx 80 - 300$ pc for nine galaxies at $z \approx 6 - 9$, while Robertson et al. (2023) provide the estimates $r_e \approx 50 - 165$ pc for four galaxies at $z \approx 10 - 13$. As highlighted by Baggen et al. (2023), these value are below the prediction of the numerical simulation by (Marshall et al. 2022), across the redshift range $z = 7$ to $z = 11$. However note that the gravitational softening of these simulations is substantial, about 240 pc at $z = 8$.

As a rough estimate of the effective radius of the stellar disk r_e , we use $r_e \simeq 1.7R_d$, where R_d is taken from eq. (13). This yields

$$r_e = 550 \text{ pc} \frac{\lambda_B}{0.035} \left(\frac{11}{1+z} \right) \left(\frac{M}{10^{11} M_\odot} \right)^{1/3}. \quad (17)$$

Adopting a normal distribution for $\ln \lambda_B$, where a mean expressed as $\ln \lambda_0$ with $\lambda_0 = 0.035$ and an rms of $\sigma = 0.55$, we find that the observational estimates are within $\approx 2 - 3\sigma$ of eq. (17).

The effective radii derived from eq. (17), including the scatter in λ_B , are broadly consistent the findings of (Marshall et al. 2022). However, these authors do not present results as a function of halo mass, preventing a direct comparison.

A clumpy disk at high redshifts may actually be subject to dynamical friction, leading to smaller disk sizes. The role of dynamical friction in the simulated galaxies of Marshall et al. (2022) remains uncertain, due to potential limitations in gravitational force resolution that may not sufficiently capture the effects of dynamical friction. The dynamical timescale of a clump of mass M_1 at a distance r from the center of the halo is $t_{\text{df}} \approx (\ln \Lambda)^{-1} M(r)/M_1 r/V_c$, where $M(r)$ is the mass of the halo contained within r (Binney & Tremaine 2008). Consider a clump of mass M_1 at a distance $r = R_d$. For an isothermal sphere $M(R_d) = M_h(R_d/r_h) = \lambda_B M_h$ and $V_c = \sqrt{GM_h/r_h}$, we find

$$t_{\text{df}} = \left(\frac{9}{\ln \Lambda} \right) \left(\frac{M_h/10^{11}}{M_1/10^7} \right) \left(\frac{\lambda_B}{0.035} \right)^2 \left(\frac{11}{1+z} \right)^{3/2} 95 \text{ Myr}, \quad (18)$$

where we have used eq. (1), $\ln \Lambda = 9$ corresponds to $M_1 = 10^7 M_\odot$ and $M_h = 10^{11} M_\odot$ (yielding a maximum impact parameter $b_{\text{max}} = r_h = 13$ kpc at $z = 10$). Therefore, dynamical friction could play an important role over the relevant dynamical timescales of high redshift galaxies.

6. SUMMARY AND DISCUSSION

The approach of constrained simulations is highly beneficial for studying rare cosmological structures. Here we have only conducted simulations with constant resolution across the entire simulation box. However, a combination of zoom-in techniques and constrained initial conditions is most appropriate for resolving rare structures as well as capturing the gravitational influence of the large scale environment.

Our simulations indicate the the average accretion history of rare halos is similar to form found for average halos in the literature. Furthermore, the accretion curves of halos show both long-term fluctuations on a 100 Myr scale and short-term variations, potentially leading to variability (stochasticity) in the associated star formation rate.

In fig. 6 we have seen that a dividing the observed SFR by a factor $f_t = 0.02$, leads to \dot{M}_h that are consistent with the simulations constrained to include a halo of mass $M_h \approx 10^{11} M_\odot$. The agreement spans the entire considered redshift range, $z > 9$. Interestingly, dividing the observed stellar masses by the same f_t yields a good

match with the halo masses in the simulations, but this is only true for $z \gtrsim 10$. For galaxies at $z \simeq 9$, the factor required is $\approx 0.004 - 0.02$, closer to what is seen in low redshift galaxies.

This peculiar behaviour can stem from challenges in accurately estimating the stellar masses. Indeed, SFRs estimated from UV magnitudes are generally more reliable than stellar mass estimates, which require assumptions about the entire star formation history (e.g. Whitler et al. 2023). Nonetheless, in the estimating the SFRs, the impact of potential uncertainties due to potential dust attenuation needs to be assessed (e.g. Kennicutt et al. 2012). However, dust attenuation is expected to be small in these high redshift galaxies (e.g. Bouwens et al. 2023), suggesting that the observed discrepancies could primarily be due to the complexities of stellar mass estimation.

Another possibility for this behaviour is an abrupt change in the conditions for star formation at $z \approx 9-10$, similar to the suggestion of Silk et al. (2024) although their model refers to transition at $z \approx 6$.

There is a wealth of studies investigating the SHMR, M_*/M_h , against the halo mass, M_h , in the literature, at redshifts $z \lesssim 10$ using pre-JWST data (e.g. Guo et al. 2010; Yang et al. 2012; Leauthaud et al. 2012; Moster et al. 2013; Rodríguez-Puebla et al. 2017; Behroozi et al. 2013; Girelli et al. 2020). These studies rely on mappings between observed stellar mass function and a halo mass function, with the latter being motivated and calibrated through N-body simulations. The two-point correlation function could also be invoked to further constrain the SHMR (e.g. Rodríguez-Puebla et al. 2013). Despite important differences among these studies, they all agree on basic features. The SHMR shows a peak at $M_h \approx 10^{12} M_\odot$ at $z \approx 0$. The peak tends to shift towards lower halo masses at high redshifts ($M_h \approx 2 \times 10^{11} M_\odot$ at $z \approx 7$). The peak SHMR does not exceeds 0.05 across $z \lesssim 10$ (Girelli et al. 2020). Moving from the peak to lower masses, the SHMR declined rapidly from a few percents at the peak to a few times 10^{-3} at $M_h \approx 10^{11} M_\odot$ at $z = 0$. Within the observational uncertainties, most studies suggest little evolution of the SHMR for redshifts below $z \approx 2$ (Rodríguez-Puebla et al. 2017), although Behroozi et al. (2013) find a decrease in the SHMR, from $z \approx 0$ to $z \approx 2$, for halo masses below. Moreover, for halos with $M_h \approx 10^{11} M_\odot$, these authors find a significant increase of the SHMR from low to high redshifts, reaching approximately 10^{-2} at $z \approx 8$.

The default implementations of semi-analytic models of galaxy formation (SAMs) imply modest changes in the SHMR with redshift for halo masses below the

peak of the SHMR, where stellar dominates AGN feedback. The Durham SAMs predict a nearly non-evolving SHMR, for $M_h \lesssim 10^{12} M_\odot$ out to $z \approx 4$, with $M_*/M_h \approx 3 \times 10^{-3}$ at $M_h \approx 10^{11} M_\odot$ (Mitchell et al. 2018). Furthermore, the Santa Cruz models, predict very little evolution of the SHMR for $M_h \lesssim 10^{11} M_\odot$ between $z = 8$ and $z = 17$, with $M_*/M_h \approx 10^{-2}$ at $M_h \approx 10^{11} M_\odot$. This trend of minimal evolution continues across the lower redshift range ($z \lesssim 6$), where the SHMR remains close to its value at higher redshifts according to the default implementation of the Santa Cruz SAMs (Somerville et al. 2015). However, comparing between the SHMR in figure 8 of (Somerville et al. 2015) to that in figure B2 in (Yung et al. 2024), reveals differences at the low mass end, specifically for $M_h \lesssim 10^{10} M_\odot$.

The question of why SAMs of galaxy formation yield a nearly invariant SHMR for halo masses below $\approx 10^{11} M_\odot$, even when SN feedback is considered less efficient at $z \gtrsim 10$ due to higher values of V_c at those epochs, is intriguing. In these models, gas expelled from the disk by stellar feedback is typically assumed to join the hot component of the circumgalactic medium (CGM). This gas eventually cools on a few dynamical timescales (e.g. Faerman et al. 2020) and settles into the disk to be reincorporated into the star formation process. In contrast, the simplified model presented here assumes that the gas ejected by SN feedback is not returned to the halo and never becomes available for star formation again. However, this process is sensitive to the circular velocity which for there same halo mass, is more

In the model outlined in §4, we have considered the circular velocity of the halo, V_c , as the parameter governing SN feedback. However, it can be argued that the maximum circular velocity (the peak of the rotation curve), V_{\max} , is more relevant since it reflects the depth of the gravitational potential of the halo.

In the regime of stable clustering, V_{\max} is expected to remain constant over long cosmic epochs. Thus, employing V_{\max} instead of V_c in the model should result in a constant SHMR over extended periods. However, we are examining halos of the same mass at different epochs. Hence, the question is whether halos within the relevant mass range, approximately $10^{11} M_\odot$, also experience moderate mass growth over cosmic time scales.

The study by (Rodríguez-Puebla et al. 2016) on the median growth of halos in MultiDark N-body simulations indicates that indeed, halos with a mass of $10^{11} M_\odot$ at redshift $z = 0$ have not significantly increased in mass since $z = 2$. For these halos, the median V_{\max} remains notably constant up to redshifts of $z = 3-4$ (refer to figures 5&6 in their paper). However,

the scenario shifts as we approach $z = 10$. The mass scale of $10^{11} M_{\odot}$ at $z = 10$ corresponds to the median mass of a halo of $10^{15} M_{\odot}$ at $z = 0$. At $z = 10$, this median halo possesses a V_{\max} of approximately 200 km/s.

7. DATA AVAILABILITY

No new data were generated or analysed in support of this research.

8. ACKNOWLEDGEMENTS

The author has benefited from fruitful conversations with Andrew Benson, Enzo Branchini, Stephane Charlot, Avishai Dekel and Joe Silk. This research is supported by a grant from the Israeli Science Foundation and a grant from the Asher Space Research Institute. The research in this paper made use of the SWIFT open-source simulation code (<http://www.swiftsim.com>, Schaller et al. (2018)) version 1.0.0.

REFERENCES

- Angulo, R. E., Springel, V., White, S. D., et al. 2012, *MNRAS*, 426, 2046, doi: [10.1111/j.1365-2966.2012.21830.x](https://doi.org/10.1111/j.1365-2966.2012.21830.x)
- Asgari, M., Lin, C. A., Joachimi, B., et al. 2021, *A&A*, 645, A104, doi: [10.1051/0004-6361/202039070](https://doi.org/10.1051/0004-6361/202039070)
- Baggen, J. F. W., van Dokkum, P., Labbé, I., et al. 2023, *ApJL*, 955, L12, doi: [10.3847/2041-8213/acf5ef](https://doi.org/10.3847/2041-8213/acf5ef)
- Behroozi, P., Conroy, C., Wechsler, R. H., et al. 2020, *MNRAS*, 499, 5702, doi: [10.1093/mnras/staa3164](https://doi.org/10.1093/mnras/staa3164)
- Behroozi, P. S., & Silk, J. 2015, *ApJ*, 799, 32, doi: [10.1088/0004-637X/799/1/32](https://doi.org/10.1088/0004-637X/799/1/32)
- Behroozi, P. S., Wechsler, R. H., & Conroy, C. 2013, *The Astrophysical Journal*, 770, 57, doi: [10.1088/0004-637X/770/1/57](https://doi.org/10.1088/0004-637X/770/1/57)
- Bennett, C. L., Larson, D., Weiland, J. L., et al. 2013, *ApJS*, 208, 20, doi: [10.1088/0067-0049/208/2/20](https://doi.org/10.1088/0067-0049/208/2/20)
- Benson, A. J. 2010, *New Astronomy*, 17, 175, doi: [10.1016/j.newast.2011.07.004](https://doi.org/10.1016/j.newast.2011.07.004)
- Binney, J., & Tremaine, S. 2008, *Galactic dynamics* (Princeton University Press), 885
- Bouwens, R. J., Stefanon, M., Brammer, G., et al. 2023, *MNRAS*, 523, 1036, doi: [10.1093/mnras/stad1145](https://doi.org/10.1093/mnras/stad1145)
- Bower, R. G., Benson, a. J., Malbon, R., et al. 2006, *MNRAS*, 370, 645, doi: [10.1111/j.1365-2966.2006.10519.x](https://doi.org/10.1111/j.1365-2966.2006.10519.x)
- Boylan-Kolchin, M. 2023, *Nature Astronomy*, 7, 731, doi: [10.1038/S41550-023-01937-7](https://doi.org/10.1038/S41550-023-01937-7)
- Bullock, J. S., Dekel, A., Kolatt, T. S., et al. 2001, *ApJ*, 555, 240, doi: [10.1086/321477](https://doi.org/10.1086/321477)
- Carrick, J., Turnbull, S. J., Lavaux, G., & Hudson, M. J. 2015, *MNRAS*, 450, 317, doi: [10.1093/mnras/stv547](https://doi.org/10.1093/mnras/stv547)
- Chandrasekhar, S. 1949, *Reviews of Modern Physics*, 21, 383, doi: [10.1103/RevModPhys.21.383](https://doi.org/10.1103/RevModPhys.21.383)
- Chen, Y., Mo, H. J., & Wang, K. 2023, *MNRAS*, 526, 2542, doi: [10.1093/mnras/stad2866](https://doi.org/10.1093/mnras/stad2866)
- Chevallard, J., & Charlot, S. 2016, *MNRAS*, 462, 1415, doi: [10.1093/mnras/stw1756](https://doi.org/10.1093/mnras/stw1756)
- Cole, J. W., Papovich, C., Finkelstein, S. L., et al. 2023, eprint arXiv:2312.10152, arXiv:2312.10152, doi: [10.48550/ARXIV.2312.10152](https://doi.org/10.48550/ARXIV.2312.10152)
- Cole, S., Percival, W. J., & Peacock, J. A. 2005, *MNRAS*, 362, 505, doi: [10.1111/j.1365-2966.2005.09318.x](https://doi.org/10.1111/j.1365-2966.2005.09318.x)
- Cora, S. A. 2006, *MNRAS*, 368, 1540, doi: [10.1111/j.1365-2966.2006.10271.x](https://doi.org/10.1111/j.1365-2966.2006.10271.x)
- Croton, D. J., Springel, V., White, S. D. M., et al. 2006, *Monthly Notices of the Royal Astronomical Society*, 365, 11, doi: [10.1111/j.1365-2966.2005.09675.x](https://doi.org/10.1111/j.1365-2966.2005.09675.x)
- Davis, M., Nusser, A., Masters, K. L., et al. 2011, *MNRAS*, 413, 2906, doi: [10.1111/j.1365-2966.2011.18362.x](https://doi.org/10.1111/j.1365-2966.2011.18362.x)
- Dekel, A., Sari, R., & Ceverino, D. 2009a, *ApJ*, 703, 785, doi: [10.1088/0004-637X/703/1/785](https://doi.org/10.1088/0004-637X/703/1/785)
- Dekel, A., Sarkar, K. C., Birnboim, Y., Mandelker, N., & Li, Z. 2023, *Monthly Notices of the Royal Astronomical Society*, 523, 3201, doi: [10.1093/mnras/stad1557](https://doi.org/10.1093/mnras/stad1557)
- Dekel, A., & Silk, J. 1986, *ApJ*, 303, 39, doi: [10.1086/164050](https://doi.org/10.1086/164050)
- Dekel, A., Birnboim, Y., Engel, G., et al. 2009b, *Nature*, 457, 451, doi: [10.1038/nature07648](https://doi.org/10.1038/nature07648)
- Despali, G., Giocoli, C., Angulo, R. E., et al. 2016, *MNRAS*, 456, 2486, doi: [10.1093/mnras/stv2842](https://doi.org/10.1093/mnras/stv2842)
- D'Eugenio, F., Maiolino, R., Carniani, S., et al. 2023, eprint arXiv:2311.09908, arXiv:2311.09908, doi: [10.48550/ARXIV.2311.09908](https://doi.org/10.48550/ARXIV.2311.09908)
- Diemer, B. 2018, *ApJS*, 239, 35, doi: [10.3847/1538-4365/aaee8c](https://doi.org/10.3847/1538-4365/aaee8c)
- Donnan, C. T., Mcleod, D. J., Dunlop, J. S., et al. 2023, *MNRAS*, 518, 6011, doi: [10.1093/mnras/stac3472](https://doi.org/10.1093/mnras/stac3472)
- Dressler, A., Rieke, M., Eisenstein, D., et al. 2024
- Eisenstein, D. J., Seo, H.-J., Sirko, E., & Spergel, D. N. 2007, *The Astrophysical Journal*, 664, 675, doi: [10.1086/518712](https://doi.org/10.1086/518712)
- El-Zant, A., Shlosman, I., & Hoffman, Y. 2001, *ApJ*, 560, 636, doi: [10.1086/322516](https://doi.org/10.1086/322516)

- Elahi, P. J., Cañas, R., Poulton, R. J., et al. 2019, Publications of the Astronomical Society of Australia, 36, e021, doi: [10.1017/pasa.2019.12](https://doi.org/10.1017/pasa.2019.12)
- Faerman, Y., Sternberg, A., & Mckee, C. F. 2020, ApJ, 893, 82, doi: [10.3847/1538-4357/ab7ffc](https://doi.org/10.3847/1538-4357/ab7ffc)
- Fakhouri, O., Ma, C. P., & Boylan-Kolchin, M. 2010, Monthly Notices of the Royal Astronomical Society, 406, 2267, doi: [10.1111/j.1365-2966.2010.16859.x](https://doi.org/10.1111/j.1365-2966.2010.16859.x)
- Ferrara, A., Pallottini, A., & Dayal, P. 2023, MNRAS, 522, 3986, doi: [10.1093/MNRAS/STAD1095](https://doi.org/10.1093/MNRAS/STAD1095)
- Finkelstein, S. L., Bagley, M., Song, M., et al. 2022, ApJ, 928, 52, doi: [10.3847/1538-4357/ac3aed](https://doi.org/10.3847/1538-4357/ac3aed)
- Fu, H., Shankar, F., Ayromlou, M., et al. 2022, MNRAS, 516, 3206, doi: [10.1093/mnras/stac2205](https://doi.org/10.1093/mnras/stac2205)
- Gardner, J. P., Mather, J. C., Abbott, R., et al. 2023, PASP, 135, doi: [10.1088/1538-3873/acd1b5](https://doi.org/10.1088/1538-3873/acd1b5)
- Girelli, G., Pozzetti, L., Bolzonella, M., et al. 2020, A&A, 634, A135, doi: [10.1051/0004-6361/201936329](https://doi.org/10.1051/0004-6361/201936329)
- Grand, R. J., Marinacci, F., Pakmor, R., et al. 2021, MNRAS, 507, 4953, doi: [10.1093/mnras/stab2492](https://doi.org/10.1093/mnras/stab2492)
- Guo, Q., White, S., Li, C., & Boylan-Kolchin, M. 2010, MNRAS, 404, 1111, doi: [10.1111/j.1365-2966.2010.16341.x](https://doi.org/10.1111/j.1365-2966.2010.16341.x)
- Harikane, Y., Nakajima, K., Ouchi, M., et al. 2024, ApJ, 960, 56, doi: [10.3847/1538-4357/ad0b7e](https://doi.org/10.3847/1538-4357/ad0b7e)
- Harikane, Y., Ouchi, M., Oguri, M., et al. 2023, ApJS, 265, 5, doi: [10.3847/1538-4365/acaaa9](https://doi.org/10.3847/1538-4365/acaaa9)
- Hellwing, W. A., Nusser, A., Feix, M., & Bilicki, M. 2017, MNRAS, 467, 2787, doi: [10.1093/mnras/stx213](https://doi.org/10.1093/mnras/stx213)
- Henriques, B. M., White, S. D., Thomas, P. A., et al. 2015, MNRAS, 451, 2663, doi: [10.1093/MNRAS/STV705](https://doi.org/10.1093/MNRAS/STV705)
- Hoffman, Y., Courtois, H. M., & Tully, R. B. 2015, MNRAS, 449, 4494, doi: [10.1093/mnras/stv615](https://doi.org/10.1093/mnras/stv615)
- Hoffman, Y., & Ribak, E. 1991, ApJL, 380, L5, doi: [10.1086/186160](https://doi.org/10.1086/186160)
- Jenkins, a. R., Frenk, C. S., White, S. D. M., et al. 2001, MNRAS, 321, 372, doi: [10.1046/j.1365-8711.2001.04029.x](https://doi.org/10.1046/j.1365-8711.2001.04029.x)
- Johnson, B. D., Leja, J., Conroy, C., & Speagle, J. S. 2021, ApJS, 254, 22, doi: [10.3847/1538-4365/abef67](https://doi.org/10.3847/1538-4365/abef67)
- Katz, N., White, S. D. M., Katz, N., & White, S. D. M. 1993, ApJ, 412, 455, doi: [10.1086/172935](https://doi.org/10.1086/172935)
- Kauffmann, G., White, S. D. M., & Guiderdoni, B. 1993, MNRAS, 264, 201, doi: [10.1093/mnras/264.1.201](https://doi.org/10.1093/mnras/264.1.201)
- Kennicutt, R. C. 1998, ApJ, 498, 541, doi: [10.1086/305588](https://doi.org/10.1086/305588)
- Kennicutt, R. C., & De Los Reyes, M. A. C. 2021, ApJ, 908, 61, doi: [10.3847/1538-4357/abd3a2](https://doi.org/10.3847/1538-4357/abd3a2)
- Kennicutt, R. C., Evans, N. J., Kennicutt, R. C., & Evans, N. J. 2012, ARA&A, 50, 531, doi: [10.1146/ANNUREV-ASTRO-081811-125610](https://doi.org/10.1146/ANNUREV-ASTRO-081811-125610)
- Krumholz, M. R., Burkhardt, B., Forbes, J. C., & Crocker, R. M. 2018, MNRAS, 477, 2716, doi: [10.1093/mnras/sty852](https://doi.org/10.1093/mnras/sty852)
- Larson, R. B. 1974, MNRAS, 169, 229, doi: [10.1093/mnras/169.2.229](https://doi.org/10.1093/mnras/169.2.229)
- Leauthaud, A., Tinker, J., Bundy, K., et al. 2012, ApJ, 744, 159, doi: [10.1088/0004-637X/744/2/159](https://doi.org/10.1088/0004-637X/744/2/159)
- Libeskind, N. I., Carlesi, E., Grand, R. J., et al. 2020, MNRAS, 498, 2968, doi: [10.1093/mnras/staa2541](https://doi.org/10.1093/mnras/staa2541)
- Lilow, R., Nusser, A., Lilow, R., & Nusser, A. 2021, MNRAS, 507, 1557, doi: [10.1093/MNRAS/STAB2009](https://doi.org/10.1093/MNRAS/STAB2009)
- Ludlow, A. D., Borzyszkowski, M., Porciani, C., et al. 2014, MNRAS, 445, 4110, doi: [10.1093/MNRAS/STU2021](https://doi.org/10.1093/MNRAS/STU2021)
- Marshall, M. A., Wilkins, S., Di Matteo, T., et al. 2022, MNRAS, 511, 5475, doi: [10.1093/mnras/stac380](https://doi.org/10.1093/mnras/stac380)
- Mason, C. A., Trenti, M., & Treu, T. 2023, MNRAS, 521, 497, doi: [10.1093/mnras/stad035](https://doi.org/10.1093/mnras/stad035)
- Mitchell, P. D., Lacey, C. G., Lagos, C. D., et al. 2018, MNRAS, 474, 492, doi: [10.1093/mnras/stx2770](https://doi.org/10.1093/mnras/stx2770)
- Mo, H. J., Mao, S., & White, S. D. 1998, MNRAS, 295, 319, doi: [10.1046/j.1365-8711.1998.01227.x](https://doi.org/10.1046/j.1365-8711.1998.01227.x)
- Moster, B. P., Naab, T., & White, S. D. 2020, MNRAS, 499, 4748, doi: [10.1093/MNRAS/STAA3019](https://doi.org/10.1093/MNRAS/STAA3019)
- Moster, B. P., Naab, T., & White, S. D. M. 2013, MNRAS, 428, 3121, doi: [10.1093/mnras/sts261](https://doi.org/10.1093/mnras/sts261)
- Nusser, A., & Silk, J. 2022, MNRAS, 509, 2979, doi: [10.1093/mnras/stab3121](https://doi.org/10.1093/mnras/stab3121)
- Okalidis, P., Grand, R. J., Yates, R. M., & Kauffmann, G. 2021, MNRAS, 504, 4400, doi: [10.1093/MNRAS/STAB1142](https://doi.org/10.1093/MNRAS/STAB1142)
- Pacifici, C., Iyer, K. G., Mobasher, B., et al. 2023, ApJ, 944, 141, doi: [10.3847/1538-4357/ACACFF](https://doi.org/10.3847/1538-4357/ACACFF)
- Pallottini, A., & Ferrara, A. 2023, A&A, 677, doi: [10.1051/0004-6361/202347384](https://doi.org/10.1051/0004-6361/202347384)
- Peebles, P. J. E. 1980, Research supported by the National Science Foundation. Princeton, N.J., Princeton University Press, 1980. 435 p.
- Pérez-González, P. G., Costantin, L., Langeroodi, D., et al. 2023, ApJL, 951, L1, doi: [10.3847/2041-8213/acd9d0](https://doi.org/10.3847/2041-8213/acd9d0)
- Planck Collaboration, Aghanim, N., Akrami, Y., et al. 2018, eprint arXiv, 1807.06209. <http://arxiv.org/abs/1807.06209>
- Press, W. H., & Schechter, P. 1974, ApJ, 187, 425, doi: [10.1086/152650](https://doi.org/10.1086/152650)
- Press, W. H., Schechter, P., Press, W. H., & Schechter, P. 1974, ApJ, 187, 425, doi: [10.1086/152650](https://doi.org/10.1086/152650)
- Puchwein, E., & Springel, V. 2013, MNRAS, 428, 2966, doi: [10.1093/mnras/sts243](https://doi.org/10.1093/mnras/sts243)
- Riess, A. G., Anand, G. S., Yuan, W., et al. 2023, ApJL, 956, L18, doi: [10.3847/2041-8213/acf769](https://doi.org/10.3847/2041-8213/acf769)

- Robertson, B. E., Kravtsov, A. V., Tinker, J., & Zentner, A. R. 2009, *ApJ*, 696, 636, doi: [10.1088/0004-637X/696/1/636](https://doi.org/10.1088/0004-637X/696/1/636)
- Robertson, B. E., Tacchella, S., Johnson, B. D., et al. 2023, *Nature Astronomy*, 7, 611, doi: [10.1038/S41550-023-01921-1](https://doi.org/10.1038/S41550-023-01921-1)
- Rodríguez-Puebla, A., Avila-Reese, V., & Drory, N. 2013, *ApJ*, 767, 92, doi: [10.1088/0004-637X/767/1/92](https://doi.org/10.1088/0004-637X/767/1/92)
- Rodríguez-Puebla, A., Behroozi, P., Primack, J., et al. 2016, *MNRAS*, 462, 893, doi: [10.1093/mnras/stw1705](https://doi.org/10.1093/mnras/stw1705)
- Rodríguez-Puebla, A., Primack, J. R., Avila-Reese, V., & Faber, S. M. 2017, *MNRAS*, 470, 651, doi: [10.1093/mnras/stx1172](https://doi.org/10.1093/mnras/stx1172)
- Schaller, M., Gonnet, P., Draper, P. W., et al. 2018, *Astrophysics Source Code Library*, ascl:1805.020. <https://ui.adsabs.harvard.edu/abs/2018ascl.soft05020S/abstract>
- Schaller, M., Borrow, J., Draper, P. W., et al. 2023, *MNRAS*, 000, 1. www.swiftsim.com.
- Schmidt, M. 1959, *ApJ*, 129, 243, doi: [10.1086/146614](https://doi.org/10.1086/146614)
- Seppi, R., Comparat, J., Nandra, K., et al. 2021, *A&A*, 652, A155, doi: [10.1051/0004-6361/202039123](https://doi.org/10.1051/0004-6361/202039123)
- Sheth, R. K., & Tormen, G. 1999, *MNRAS*, 308, 119, doi: [10.1046/j.1365-8711.1999.02692.x](https://doi.org/10.1046/j.1365-8711.1999.02692.x)
- Shuntov, M., McCracken, H. J., Gavazzi, R., et al. 2022, *A&A*, 664, A61, doi: [10.1051/0004-6361/202243136](https://doi.org/10.1051/0004-6361/202243136)
- Silk, J., Begelman, M. C., Norman, C., Nusser, A., & Wyse, R. F. G. 2024, *ApJL*, 961, L39, doi: [10.3847/2041-8213/AD1BF0](https://doi.org/10.3847/2041-8213/AD1BF0)
- Silk, J., & Rees, M. J. 1998, *A&A*, 331, L1. <https://ui.adsabs.harvard.edu/abs/1998A%26A...331L...1S/abstract>
- Somerville, R. S., & Davé, R. 2015, *ARAA*, 53, 51, doi: [10.1146/annurev-astro-082812-140951](https://doi.org/10.1146/annurev-astro-082812-140951)
- Somerville, R. S., Popping, G., & Trager, S. C. 2015, *MNRAS*, 453, 4337, doi: [10.1093/MNRAS/STV1877](https://doi.org/10.1093/MNRAS/STV1877)
- Sun, G., Faucher-Giguère, C. A., Hayward, C. C., & Shen, X. 2023a, *MNRAS*, 526, 2665, doi: [10.1093/mnras/stad2902](https://doi.org/10.1093/mnras/stad2902)
- Sun, G., Faucher-Giguère, C.-A., Hayward, C. C., et al. 2023b, *ApJL*, 955, L35, doi: [10.3847/2041-8213/acf85a](https://doi.org/10.3847/2041-8213/acf85a)
- Tegmark, M., Blanton, M. R., Strauss, M. A., et al. 2004, *The Astrophysical Journal*, 606, 702, doi: [10.1086/382125](https://doi.org/10.1086/382125)
- Tinker, J., Kravtsov, A. V., Klypin, A., et al. 2008, *The Astrophysical Journal*, 688, 709, doi: [10.1086/591439](https://doi.org/10.1086/591439)
- Wang, B., Leja, J., Labbé, I., et al. 2023, *ApJS*, 270, 12, doi: [10.3847/1538-4365/ad0846](https://doi.org/10.3847/1538-4365/ad0846)
- Wang, H., Mo, H. J., Yang, X., et al. 2016, *ApJ*, 831, 164, doi: [10.3847/0004-637x/831/2/164](https://doi.org/10.3847/0004-637x/831/2/164)
- White, S. D. M., & Frenk, C. S. 1991a, *ApJ*, 379, 52, doi: [10.1086/170483](https://doi.org/10.1086/170483)
- . 1991b, *ApJ*, 379, 52, doi: [10.1086/170483](https://doi.org/10.1086/170483)
- Whitler, L., Stark, D. P., Endsley, R., et al. 2023, *MNRAS*, 519, 5859, doi: [10.1093/mnras/stad004](https://doi.org/10.1093/mnras/stad004)
- Yang, H., Gao, L., Frenk, C. S., et al. 2023, *MNRAS*, 518, doi: [10.1093/mnras/stac3335](https://doi.org/10.1093/mnras/stac3335)
- Yang, X., Mo, H. J., Van Den Bosch, F. C., Zhang, Y., & Han, J. 2012, *ApJ*, 752, 41, doi: [10.1088/0004-637X/752/1/41](https://doi.org/10.1088/0004-637X/752/1/41)
- Yung, L. Y., Somerville, R. S., Finkelstein, S. L., Popping, G., & Davé, R. 2019, *MNRAS*, 483, 2983, doi: [10.1093/mnras/sty3241](https://doi.org/10.1093/mnras/sty3241)
- Yung, L. Y. A., Somerville, R. S., Finkelstein, S. L., Wilkins, S. M., & Gardner, J. P. 2024, *MNRAS*, 527, 5929, doi: [10.1093/mnras/stad3484](https://doi.org/10.1093/mnras/stad3484)